

Removing defects from sputter damage on InGaP surfaces using thermal atomic layer etching



Cite as: J. Vac. Sci. Technol. A 42, 062602 (2024); doi: 10.1116/6.0003899

Submitted: 12 July 2024 · Accepted: 5 September 2024 ·

Published Online: 4 October 2024



Ross Edel,¹ Ezra Alexander,² Taewook Nam,^{1,a)} Andrew S. Cavanagh,¹ Troy Van Voorhis,² and Steven M. George^{1,b)}

AFFILIATIONS

¹Department of Chemistry, University of Colorado, Boulder, Colorado 80309

²Department of Chemistry, Massachusetts Institute of Technology, Cambridge, Massachusetts 02139

Note: This paper is part of the Special Topic Collection Honoring John Ekerdt's Contributions to Chemical Reaction Engineering and Surface Chemistry for Electronic Materials.

^{a)}**Also at:** Department of Semiconductor Systems Engineering, Sejong University, Seoul 05006, South Korea.

^{b)}**Electronic mail:** Steven.George@colorado.edu

ABSTRACT

Thermal atomic layer etching (ALE) was utilized to remove sputter damage from InGaP samples. Removal of sputter damage from InGaP surfaces was measured using x-ray photoelectron spectroscopy (XPS). Damage was identified by the shifted doublets in the P 2p region of the XPS spectrum. Density functional theory identified the damage as corresponding to the undercoordinated atoms in the InGaP lattice. InGaP substrates were sputtered with Ar⁺ ions at 500 eV or 2 keV as a model system to simulate the exposure of InGaP to energetic species during plasma processing. The InGaP thermal ALE process used sequential exposures of hydrogen fluoride for fluorination and either trimethylaluminum or dimethylaluminum chloride for ligand exchange at 300 °C. The XPS spectra revealed that InGaP thermal ALE successfully removed damage from sputtering. The area of the shifted doublets in the P 2p region was progressively reduced versus the number of ALE cycles. After ALE, the resulting XPS spectra were equivalent to the spectrum of an InGaP sample with no sputter damage. A bulklike XPS spectrum showing minimal damage was recovered after 50 ALE cycles for a sample initially exposed to 500 eV sputtering. Sputtering at 2 keV required 100 ALE cycles to largely remove the surface defects. The etch depth consistent with 100 ALE cycles indicated a damaged material depth of ~5–6 nm. In addition, Auger electron spectroscopy (AES) revealed that the Ar AES signal from implanted Ar in InGaP after sputtering was also progressively removed versus the number of ALE cycles.

Published under an exclusive license by the AVS. <https://doi.org/10.1116/6.0003899>

I. INTRODUCTION

Aluminum indium gallium phosphide (AlInGaP) is widely used for red light-emitting diode (LED) devices.^{1,2} Surface defects on LED devices can lead to nonradiative electron/hole pair recombination that reduces their light output.³ This light quenching effect is more severe for smaller micro-LED devices that have high surface-to-volume ratios. In particular, AlInGaP devices have a higher surface recombination velocity than III-nitride materials and are more susceptible to a drop in external quantum efficiency with decreasing device scale.^{4–7} Cathodoluminescence mapping of a $6 \times 6 \mu\text{m}^2$ AlGaInP mesa structure showed a drop in efficiency across ~85% of the structure area.⁸

Modeling indicates that the decrease in quantum efficiency for small devices is a result of defects near the sidewalls serving as traps

and reducing the concentration of charge carriers.^{9–11} The fabrication of micro-LED devices typically involves reactive ion etching (RIE) to form the mesa structures that emit light.¹² RIE requires physical sputtering of the surface to desorb reaction products.¹³ Surface defects are believed to be formed by the energetic ion species employed in the RIE process. Lattice distortion penetrating a few nanometers below the surface as a result of RIE has been directly observed by high resolution transmission electron spectroscopy of AlInGaP mesas¹⁴ and by scanning transmission electron microscopy of III-nitride structures.¹⁵ Other ellipsometry studies have observed larger damage layer thicknesses for sputtered InP surfaces.¹⁶

X-ray photoelectron spectroscopy (XPS) measures electron binding energies in the near-surface region of substrates that may

10 October 2024 05:44:36

be affected by sputter damage.¹⁷ XPS can be used as a probe of damage in the near-surface region. XPS can also be employed to verify the removal of damage. For P-containing compounds, shifts in the P 2p XPS spectrum have been observed for sputter-etched InP surfaces.¹⁸ Similar shifts in the P 2p XPS spectrum are observed after the sputtering of GaAs/GaInP interfaces.¹⁹ XPS studies can also evaluate sputter damage of other materials such as TiC-coatings²⁰ and W-S thin films.²¹ A correlation between the shifts in the XPS spectra and the underlying material structure can be established using electronic structure calculations.²² Density functional theory (DFT) can be used for the assignment and interpretation of XPS spectra due to its advantageous computational scaling for large systems.

The surface defects created by sputter damage can be removed by etching procedures. Wet chemical treatments have successfully mitigated the size effect of lost quantum efficiency with miniaturization by removing or passivating the surface defects.^{14,23–29} However, a dry etch process that can remove damaged material with atomic layer precision would be more desirable in practice. One possible dry etch process is thermal atomic layer etching (ALE).³⁰ Thermal ALE is similar to the reverse of atomic layer deposition (ALD).^{31,32}

Thermal ALE involves two sequential self-limiting surface reactions.³⁰ One reaction modifies the surface layer. The second reaction volatilizes the modified surface layer. Unlike plasma ALE,³³ thermal ALE does not employ energetic species or physical sputtering to release the etch products. As a result, thermal ALE is

expected to allow gentle etching with atomic layer precision without damaging or modifying the bulk material underneath the surface layer. Thermal ALE could serve as a surface treatment to remove defects after the mesa structure is formed using RIE during micro-LED fabrication.

In this paper, XPS investigations are employed to study the removal of defects from sputter damage on InGaP surfaces using thermal ALE. InGaP ternary phosphide is used as a model for AlInGaP quaternary phosphide. Sputtering of InGaP with Ar⁺ ions is used as an analog for the exposure to energetic species that takes place during the RIE process. DFT was implemented to establish the connection between the XPS spectrum and the surface damage. These calculations concentrated on the P 2p region of the XPS spectrum. Auger electron spectroscopy (AES) was also utilized to detect the implanted Ar from the sputtering process and to measure its removal during thermal ALE. These techniques revealed that the sputter damage of InGaP can be measured by detecting the under-coordinated atoms in the InGaP lattice with XPS and that thermal ALE can progressively remove these surface defects.

II. EXPERIMENT

A. Vacuum reactor

The experiments were performed in a new three-component vacuum apparatus for *in vacuo* thermal ALE, sputtering, and AES. Figure 1 shows a schematic of this vacuum instrument.

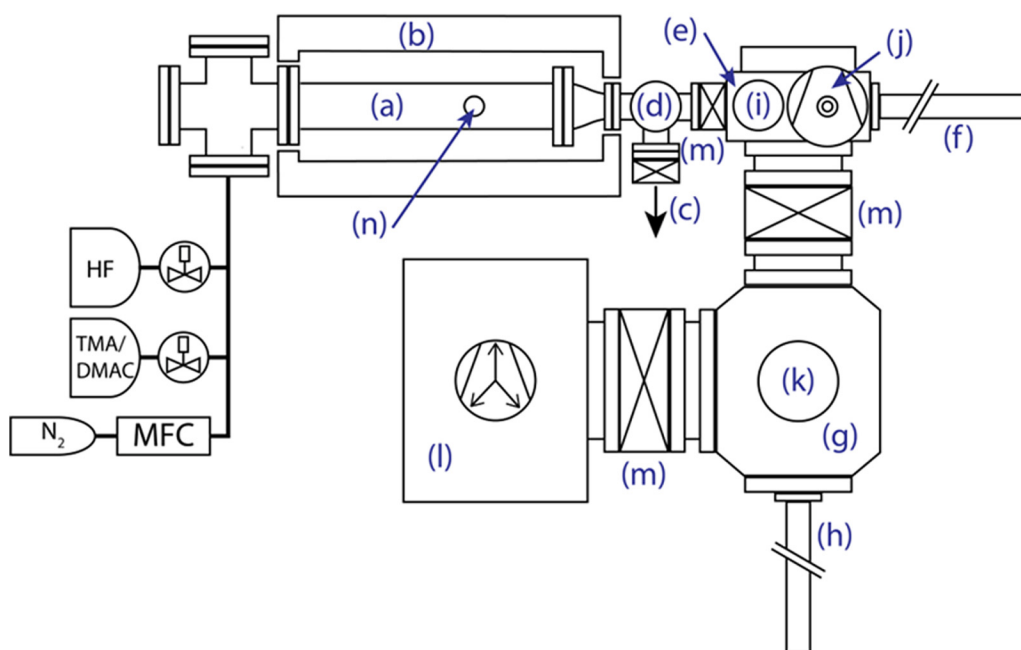


FIG. 1. Schematic of a vacuum apparatus comprised of an ALE hot-wall reactor (a) with a ceramic heater (b) that is pumped by a mechanical pump (c). Reactor pressure is monitored by a capacitance monometer (d). The vacuum apparatus also contains a load lock/sputtering chamber (e) where samples can be moved from the reactor using a magnetically coupled transfer arm (f). Samples can be transported to an AES UHV chamber (g) using another magnetically coupled transfer arm (h). The load lock chamber also contains a sputter gun (i) and is pumped by a turbopump (j). AES chamber contains a cylindrical mirror analyzer (k) and is pumped by an ion pump (l). Gate valves (m) separate the three components of the vacuum apparatus.

10 October 2024 05:44:36

One component was a hot-wall ALE reactor [Fig. 1(a)].³⁴ The reactor was heated using ceramic heaters [Fig. 1(b)]. The temperature was held at a process temperature of 300 °C with a proportional-integral-derivative temperature controller (Eurotherm 2604). The reactor was pumped with a mechanical rotary vane pump [2010C1, Pfeiffer, Fig. 1(c)]. The reactor pressure was monitored with a capacitance manometer [Baratron 121A, MKS, Fig. 1(d)]. The base pressure of the reactor was maintained at 20 mTorr without gas flow and 1 Torr with a constant flow of ultra-high purity (UHP) grade nitrogen (N₂) gas (99.999%, Airgas).

The second component of the apparatus was a load lock chamber [Fig. 1(e)]. Samples could be loaded into the hot-wall reactor using linear magnetic sample transfer [Fig. 1(f)] from this load lock chamber. Samples could also be transferred to the AES analysis chamber [Fig. 1(g)] from the load lock chamber using linear magnetic sample transfer [Fig. 1(h)]. The load lock chamber also was equipped with an ion sputter gun [PHI 04-161, Fig. 1(i)]. The load lock chamber was maintained at a base pressure of $\leq 1 \times 10^{-7}$ Torr by a turbopump [Pfeiffer Vacuum HiPace 80, Fig. 1(j)].

The third component of the apparatus was an AES analysis chamber. AES was performed using a cylindrical mirror analyzer spectrometer [PHI 10-155, Fig. 1(k)] located in an ultrahigh vacuum (UHV) chamber attached to the load lock. AES spectra were collected using a beam voltage of 3 keV and a drain current to the sample of 1–2 μ A. Analysis was performed using AugerScan software (RBD Instruments) that used peak heights of the differentiated spectrum. Sensitivity factors were provided by the AugerScan software database. In the case of Ar, a calculated sensitivity factor was derived from the ionization cross section.³⁵ The UHV chamber was maintained at a base pressure of $\leq 5 \times 10^{-10}$ Torr by an ion pump [Gamma Vacuum TiTan, Fig. 1(l)]. The three vacuum chambers were isolated with gate valves [VAT, Fig. 1(m)].

B. Samples, sputtering, and spectroscopic ellipsometry

All InGaP samples were obtained from the same 4-in. wafer. This wafer contained a 950 nm epitaxial layer of InGaP grown using metal-organic chemical vapor deposition on a GaAs substrate. The wafer was diced into 1×1 cm² coupons. The coupons were then cut in half with a diamond scribe to better fit the sample holder [Fig. 1(n)] in the ALE reactor.

The InGaP samples were either sputtered at 500 eV under 5×10^{-5} Torr of Ar for 30 min or at 2 keV under 5×10^{-5} Torr of Ar for 15 min in the load lock chamber. In both cases, the drain current during the sputter process was ~ 7 μ A. The sputter spot was intentionally defocused to cover an area ~ 1.5 cm in diameter. This area was large enough to sputter the entire InGaP sample.

Small spot ellipsometry was used to map a Si sample covered with an Al₂O₃ ALD film with a thickness of ~ 1 nm that was then sputtered at 500 eV. These measurements confirmed sputter erosion over a >1 cm² area. In addition, a visible change in appearance was always apparent after sputtering across all parts of the InGaP samples not covered by the sample holder clips. This visible change confirmed the successful sputtering of each sample. Spectroscopic ellipsometry was performed using an *ex situ*

instrument (J.A. Woollam M-2000) with automated measurements at variable incidence angles. The data were analyzed using COMPLETEEASE software (J.A. Woollam) with a GenOsc model.³⁶

C. XPS analysis

XPS analysis was performed using a PHI 5600 spectrometer with a monochromatic Al K _{α} x-ray source (1486.6 eV). Survey scans were collected with a pass energy of 93.9 eV and a step size of 0.400 eV. Detailed scans of the P 2p region were collected with a pass energy of 2.95 eV and a step size of 0.025 eV. Peak analysis was conducted using CasaXPS (Casa Software). All peaks were calibrated to the C 1s peak binding energy of 284.8 eV.

The peaks were fit using Gaussian–Lorentzian (70–30) line shapes after a Shirley background subtraction. All doublets in the P 2p region of the XPS spectrum were fit with a splitting energy of 0.86 eV. The binding energy shifts relative to the bulk doublet and full width at half maximum (FWHM) values were constrained in accordance with the DFT results and control spectra of the samples before and after sputtering.

D. Atomic layer etching

ALE was performed in the hot-wall ALE reactor.³⁴ Between static precursor doses, the reactor was evacuated by a rotary vane mechanical pump until the pressure reached the base pressure. Then, the reactor was purged with a flow of 200 SCCM of UHP N₂. The flowing N₂ gas produced a pressure of ~ 1 Torr in the reactor during the purge step. The precursors used during etching were trimethylaluminum (TMA) (Sigma-Aldrich), dimethylaluminum chloride (DMAC) (EMD Group), and hydrogen fluoride (HF) derived from HF-pyridine (70 wt. % HF, Sigma-Aldrich). HF-pyridine was transferred to a gold-plated stainless-steel bubbler under dry N₂ in a glovebox.

Atomic layer etching was performed using two processes, both of which involved static dosing at 300 °C with 60 s of purging with N₂ between precursor doses. The first process employed a 10 s dose of HF at 500 mTorr followed by a 5 s dose of TMA at 500 mTorr. This process was adapted from a previous work optimizing Al₂O₃ ALE with static exposures.³⁷ The HF/TMA process is effective for the ALE of compounds composed of elements that form stable, low volatility fluorides and have volatile methyl compounds.^{38–40} The second process substituted DMAC for TMA, with a 10 s dose of HF at 200 mTorr followed by a 5 s dose of DMAC at 750 mTorr. The HF/DMAC process is effective for the ALE of compounds composed of elements that form stable, low volatility fluorides and have volatile methyl or chloride compounds.^{39,41,42} The HF/TMA and HF/DMAC processes should be applicable for the thermal ALE of both InGaP and AlInGaP.

The HF/TMA process was sufficient for etching InGaP native oxide. In contrast, the HF/DMAC process was found to be more effective for etching bulk crystalline InGaP. This finding was consistent with a previous study showing that the chlorine ligand in DMAC was necessary to volatilize In and Ga and successfully etch InGaAs with HF/DMAC.⁴² In addition, etching with only HF/DMAC exposures often produced a chemically distinct top layer due to a conversion mechanism.⁴³ This conversion

could be avoided by first removing InGaP native oxide using sequential HF and trimethylaluminum (TMA) exposures.

All InGaP thermal ALE processing used 25 cycles of HF/TMA to remove any oxide top layer. These HF/TMA cycles were then followed by a variable number of cycles of HF/DMAC unless noted otherwise. Between each ALE experiment, the reactor walls were passivated with 10–50 nm of Al₂O₃ deposited by ALD with TMA and water at 300 °C.

E. Computation of XPS spectrum

InGaP nanocrystals were used as models to enable computational assignment of damaged and undamaged InGaP XPS spectra with atomistic detail. As opposed to periodic slab models, nanocrystal models have the advantage of capturing a variety of different surface facets, intersections of surface facets, and irregular surface moieties that may appear in sputtered InGaP samples. Structures were carved from the InP bulk crystal with specified size (up to 2.4 nm in diameter) and shape using a well-established construction procedure.^{44,45} Surfaces were then passivated with atomic halide ligands. Half of the indium atoms in the nanocrystal were randomly selected to be substituted for gallium. Structures were then fully optimized at the PBE/DZVP-MOLOPT-GTH level of theory until they converged by CP2K default thresholds.⁴⁶

The calculation of XPS spectra was conducted within the ΔSCF framework⁴⁷ using density functional theory in the Q-Chem software package.⁴⁸ Core-ionized states were converged directly using the maximum overlap method.⁴⁹ Within this framework, the cluster models were required to be charge neutral to properly capture the photoionization process. Benchmarking was performed on data sets of P 2p XPS data for small molecules in the gas phase⁵⁰ as well as on smaller nanocrystal models. This benchmarking found that the range-separated hybrid functional HSE06^{51,52} provided good core-electron binding energies (CEBEs) while greatly reducing convergence errors. The def2-svp basis set^{53–57} was employed here with basis functions on phosphorus atoms manually uncontracted to improve the description of core orbitals.⁴⁹

To reduce the computational cost, spectra were constructed by first selecting a random third of the atoms of the target element. The CEBEs of their lowest energy target 2p orbital were then computed for each of the selected atoms. For the P 2p XPS spectra, each CEBE was then used as the center of a Voigt profile to approximate homogenous spectral broadening. The parameterization of the Voigt profile was chosen to best match the FWHM between Figs. 2(a) and 3(a). A spin-orbit splitting of 0.86 eV was used in fitting the experimental results. This same spin-orbit splitting was also applied to the DFT results to generate a proper doublet.^{58,59}

The fitting of experimental P 2p XPS spectra needs to capture both homogenous broadening arising from the lifetime of the excited state and inhomogeneous broadening arising from phosphorus in distinct chemical environments. Inhomogeneous broadening is explicitly included in this DFT approach using InGaP nanocrystals. The two shifted doublets will not have the same FWHM as the bulk doublet. This arises from the fact that the shifted doublets arise from surface features. The surface features have a more varied chemical environment than the bulk features that comprise the main doublet.

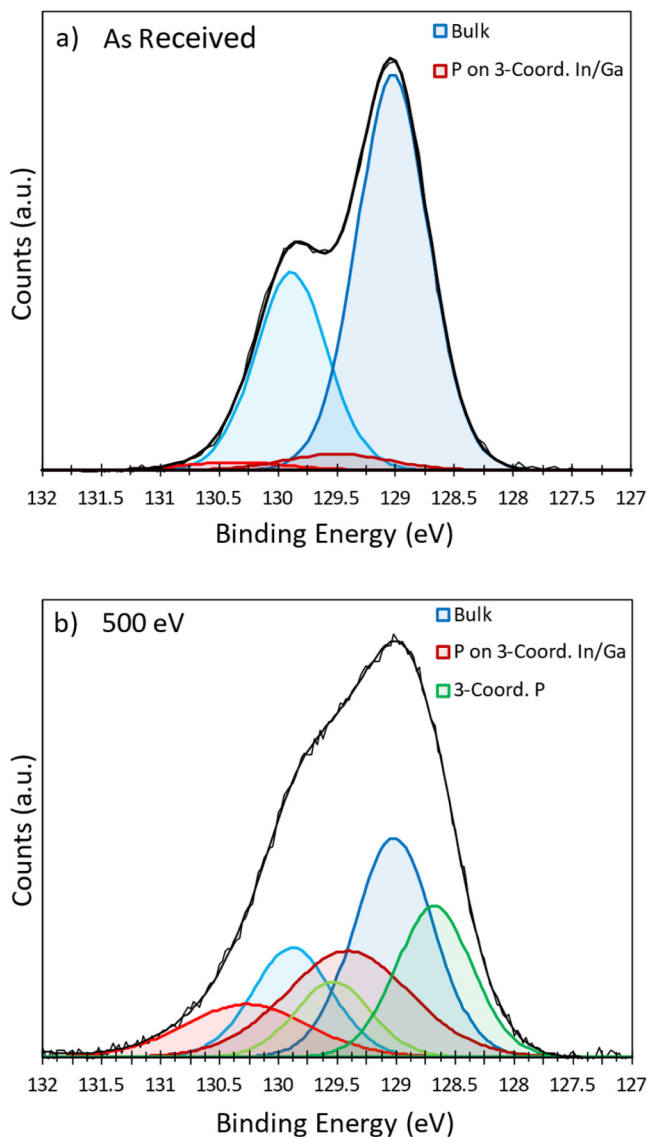


FIG. 2. XPS spectra of the P 2p region of (a) an as-received InGaP sample showing bulk doublet and (b) a sample after sputtering with 500 eV Ar⁺ ions for 30 min showing bulk doublet as well as two shifted doublets. The doublet shifted to higher CEBE corresponds to P bound to an undercoordinated In or Ga atom ("P on 3-coord. In/Ga") and the doublet shifted to lower CEBE corresponds to undercoordinated P ("3-coord. P").

III. RESULTS AND DISCUSSION

A. As-received and sputtered InGaP samples

Figure 2(a) shows an experimental XPS spectrum of the P 2p region for an as-received InGaP sample with no sputtering or processing. The bulk doublet at ~129.0 and ~129.9 eV comprises 94% of the total area with a small amount of a possible shifted doublet

10 October 2024 05:44:36

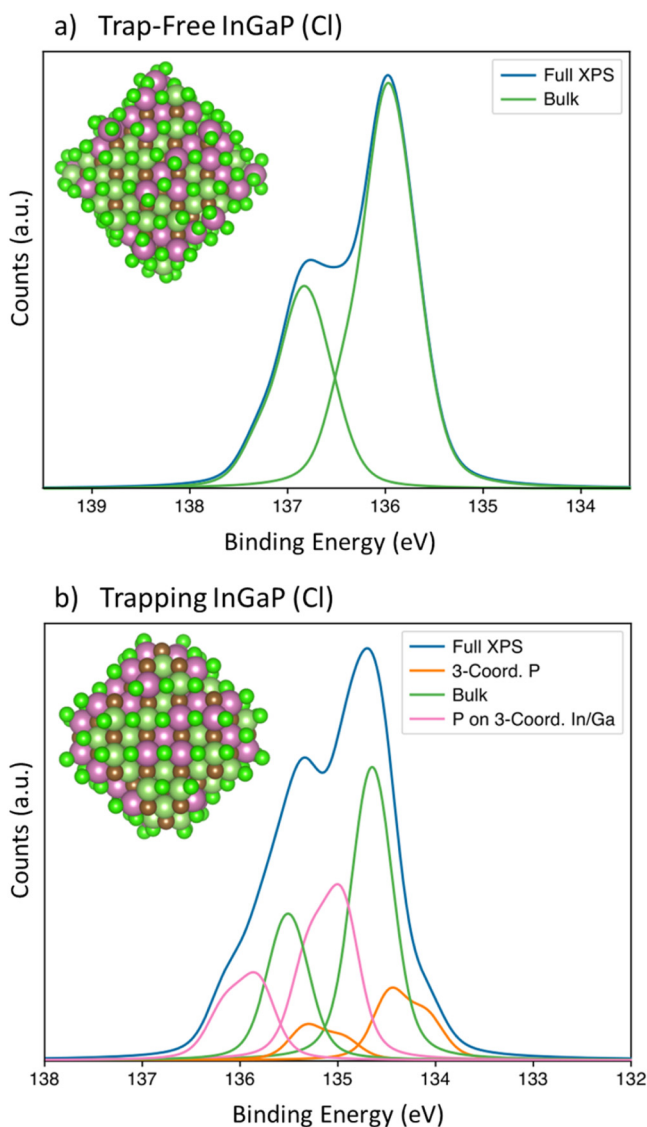


FIG. 3. Simulated P 2p XPS spectra of InGaP nanocrystals (a) without and (b) with undercoordinated surface atoms. For each doublet, the $2p_{1/2}$ contribution corresponds to a higher CEBE peak and the $2p_{3/2}$ contribution corresponds to a lower CEBE peak. Space-filling models of two nanocrystals are inset in their respective spectra, with pink atoms corresponding to indium, light green atoms corresponding to gallium, brown atoms corresponding to phosphorus, and bright green atoms corresponding to chlorine. (Color online).

at higher energy. This small amount of the shifted doublet may indicate an imperfection in the as-received crystal structure after air exposure or may be the result of an experimental error in XPS characterization.

Figure 2(b) displays an XPS scan of another InGaP sample after sputtering with Ar^+ ions for 30 min at 500 eV with no further

modification other than air exposure during transfer between instruments. In addition to the bulk doublet, two additional shifted doublets are visible with one shifted to higher binding energy and one shifted to lower energy. As a result, the bulk doublet has been reduced to 34% of the total fit area.

DFT indicates that the higher energy doublet corresponds to phosphorus bound to undercoordinated In or Ga. This higher energy doublet is shifted relative to the bulk doublet by ~ 0.40 eV. DFT also reveals that the lower energy doublet corresponds to undercoordinated phosphorus. This lower energy doublet is shifted relative to the bulk doublet by ~ 0.35 eV.

When fitting the experimental data for the shifted doublets in CASAXPS, the DFT results were used as a guide to limit the range of allowed binding energies. Both binding energy shifts were constrained to approximately match the shifts predicted by DFT within ± 0.1 eV. The FWHM values for the bulk doublet were constrained to < 0.8 eV based on the FWHM measured for unspattered samples such as Fig. 2(a). DFT calculations predict that the two shifted doublets have somewhat broader FWHMs than the bulk doublet. In particular, a better fit was obtained when the doublet shifted to higher energy was constrained to a larger FWHM of < 1.2 eV while the low energy doublet remained at < 0.8 eV.

Figure 3 shows simulated P 2p XPS spectra for two InGaP nanocrystals computed within the ΔSCF framework. For both spectra, the entire spectrum has been shifted to a higher CEBE relative to bulk InGaP. This higher CEBE is an effect arising from the finite size of these nanocrystals and the high density of electron-withdrawing Cl^- ligands used to passivate their surfaces. Despite these effects, the relative shift of the individual doublets in each spectrum is expected to mirror those in the bulk sample.

The XPS spectrum for a nanocrystal corresponding to undamaged InGaP ($\text{In}_{80}\text{Ga}_{79}\text{P}_{104}\text{Cl}_{165}^{0+}$) is displayed in Fig. 3(a). This nanocrystal is a cuboctahedron 2.6 nm in diameter displaying (100) and (111) facets on the surface. The structure was created by growing layers of In/Ga on the top of each P-terminated facet. Subsequently, all In/Ga was passivated with chlorine until achieving charge neutrality. The nanocrystal contains no indium, gallium, or phosphorus atoms with a coordination number of less than four.

The computed XPS spectrum in Fig. 3(a) contains only a single doublet, in agreement with the experimental XPS spectra of undamaged samples. Note that the “bulk” doublet contains contributions from fully coordinated phosphorus both on the surface of the nanocrystal and in the core of the nanocrystal and is, therefore, not fully symmetric. Due to the higher density of chlorine in this structure and the finite size of the models, the bulk binding energy of this undamaged sample has been shifted to a higher energy than the bulk binding energy of the damaged nanocrystal described below.

The XPS spectrum for a nanocrystal corresponding to damaged InGaP ($\text{In}_{68}\text{Ga}_{67}\text{P}_{104}\text{Cl}_{93}^{0+}$) is shown in Fig. 3(b). This nanocrystal is a truncated cuboctahedron 2.2 nm in diameter displaying (100), (110), and (111) facets on the surface. The structure contains 7 three-coordinate In/Ga and 24 three-coordinate phosphorus. The computed spectrum contains three clear doublets: a bulk doublet, a higher energy doublet shifted by 0.44 eV, and a lower energy doublet shifted by 0.33 eV. These shifts are in good agreement with those used to fit the experimental XPS spectra. Analogous features appear

10 October 2024 05:44:36

in the calculated XPS spectra of a wide range of trapping nanocrystals shown later.

The higher energy doublet arises entirely from phosphorus atoms that are directly bound to three-coordinate indium or gallium. These phosphorus atoms are the main source of electron trap states in these nanocrystals.⁶⁰ Similarly, the lower energy doublet arises entirely from three-coordinate phosphorus. These phosphorus atoms are the main source of hole trap states in these nanocrystals. The bulk peak is composed of phosphorus atoms that do not satisfy either of these criteria. Note also that the two doublets associated with surface features are broader than the bulk doublet. In fact, a splitting can be observed within each peak. Our nanocrystal models have more than one type of both three-coordinate phosphorus and phosphorus bound to three-coordinate indium/gallium. Slight differences in their electrostatic environments give rise to a splitting in their CEBEs.

B. Etch rates for InGaP thermal ALE

Bulk InGaP etch rates were determined by measuring the change in the InGaP layer thickness of unspattered InGaP reference samples after ALE using spectroscopic ellipsometry as shown in Fig. 4. Inconsistent results were obtained when attempting to measure the thickness of spattered InGaP samples with ellipsometry. These inconsistencies may be related to the inhomogeneity of the spattered layer and variable amounts of air exposure prior to ellipsometry measurements. Consequently, etched thicknesses for spattered samples have been estimated using the etch rate from the

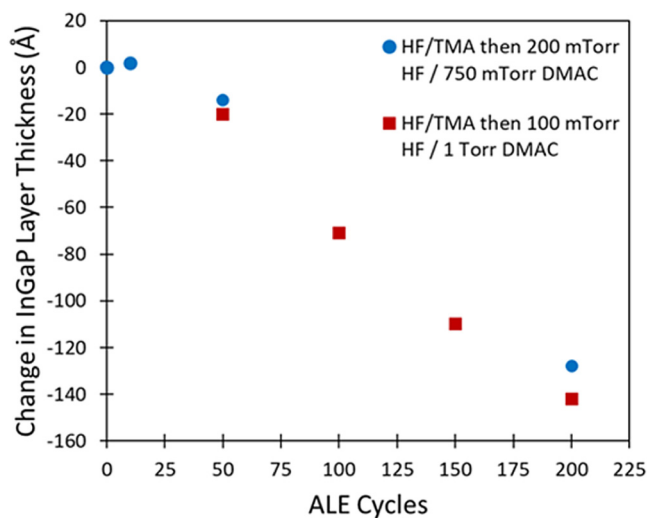


FIG. 4. Change in InGaP layer thickness of unspattered reference InGaP samples as measured by spectroscopic ellipsometry using either the standard process with 25 cycles of 500 mTorr HF/500 mTorr TMA followed by 200 mTorr HF/750 mTorr DMAC or an alternative process with 25 cycles of 500 mTorr HF/500 mTorr TMA followed by 100 mTorr HF/1 Torr DMAC. The oxide layer thickness is not included in the InGaP layer thickness. A bulk InGaP etch rate of ~ 0.7 Å/cycle is observed after removing the native oxide.

unspattered samples. Because the spattered samples do not have a native oxide, the etch rate of interest is the bulk InGaP etch rate.

The sensitivity of the etch rate to precursor pressures for static etching at 300 °C was tested by comparing the standard process of 25 cycles of 500 mTorr HF/500 mTorr TMA followed by a variable number of cycles of 200 mTorr HF/750 mTorr DMAC to an alternative process of 25 cycles of 500 mTorr HF/500 mTorr TMA followed by a variable number of cycles of 100 mTorr HF/1 Torr DMAC. Similar etch rates were found for both processes within ± 0.1 Å/cycle. These similar etch rates indicate that the etch rate is not highly sensitive to changes in precursor pressures in this regime.

As displayed in Fig. 4, a bulk InGaP etch rate of ~ 0.7 Å/cycle is obtained after the removal of the native oxide. The data point at ten ALE cycles shows no significant change in InGaP bulk layer thickness. This behavior is expected because these 10 HF/TMA ALE cycles are removing the oxide. *In vacuo* AES analysis confirms that the oxide is completely removed after 25 cycles of the HF/TMA process. The HF/TMA process alone was found to be ineffective at etching the bulk InGaP material. Consequently, the HF/TMA process is not expected to contribute significantly to the bulk InGaP etch rate.

Etched bulk InGaP thicknesses for spattered samples have been estimated by multiplying the number of HF/DMAC cycles by an etch rate of 0.7 Å/cycle. The initial 25 cycles of HF/TMA are assumed to remove any oxidized material without significantly etching the underlying InGaP material. The true etch rates for spattered materials may be higher for both processes resulting from the disruption of the crystal lattice. However, the XPS results are consistent with the etch rate remaining roughly the same for spattered and unspattered materials.

C. XPS results after different sputtering conditions and number of ALE cycles

Figure 5(a) shows the XPS spectrum for a sample that was sputtered with Ar⁺ ions at 500 eV and then processed with 50 ALE cycles at 300 °C. The XPS spectrum shows that the damaged material has been entirely removed by ALE processing. After ALE, the bulk components comprise 96% of the fit envelope, closely matching the as-received sample shown in Fig. 2(a). This finding is supported by the *in vacuo* AES results that did not detect any remaining implanted Ar after the ALE process.

Figure 5(b) displays the XPS spectrum for a sample that was annealed in the reactor under ~ 1 Torr of purging N₂ for 72 h at 300 °C after sputtering with Ar⁺ ions at 500 eV. Previous work has shown improvements in external quantum efficiency with annealing.^{24,25} Figure 5(b) shows some improvement with the bulk components rising from 35% to 64% of the total envelope area after annealing. However, annealing alone was not effective at completely removing damage. ALE was required to recover a bulk-like XPS spectrum. AES, likewise, detected remaining implanted Ar after annealing.

Figure 6(a) shows that the XPS spectrum for a 2 keV sputtered sample after 100 cycles of etching has largely been restored to a bulklike spectrum. In this case, the bulk doublet comprises 88% of the total area. Based on the bulk InGaP etch rate of ~ 0.7 Å/cycle

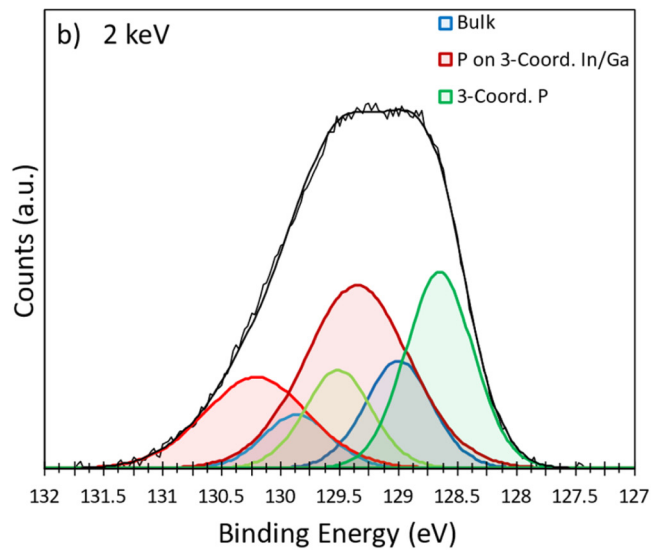
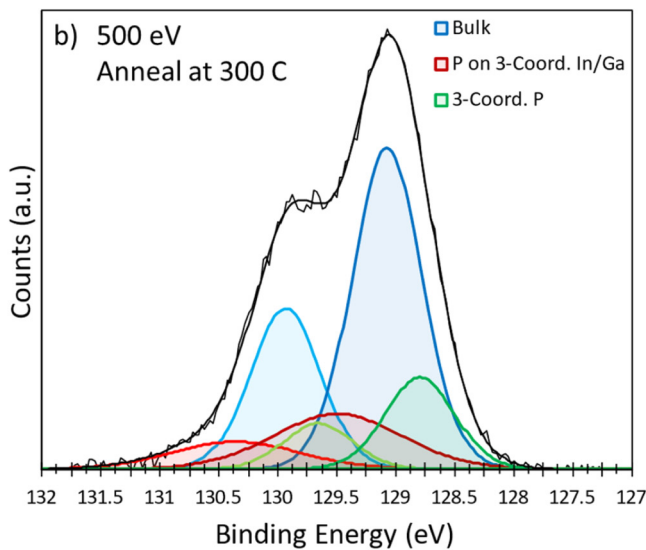
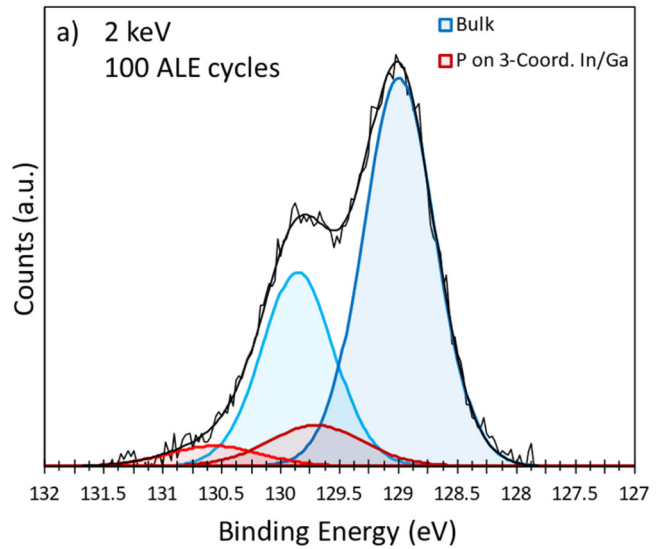
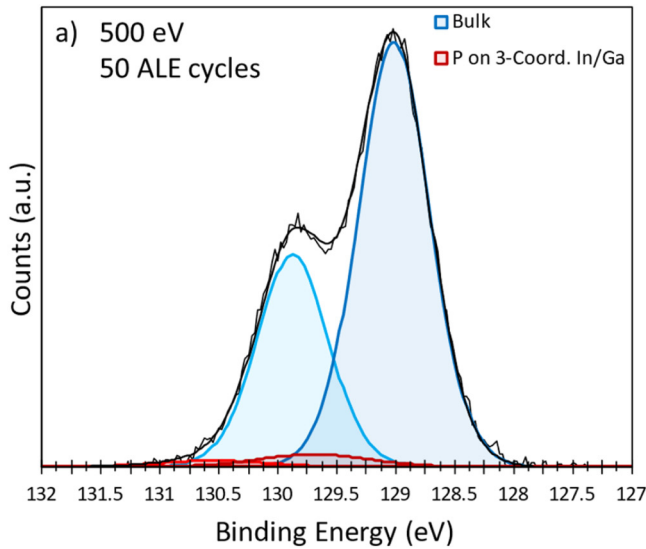


FIG. 5. (a) XPS spectrum of the P 2p region for an InGaP sample sputtered at 500 eV and then etched using 50 total ALE cycles at 300 °C. The 50 ALE cycles were 25 cycles of the HF/TMA process followed by 25 cycles of the HF/DMAC process. Bulk doublet is 96% of the total area indicating the removal of sputter damage. (b) XPS spectrum of an InGaP sample sputtered at 500 eV and then annealed in the reactor at 300 °C under 200 SCCM flow of N₂ for 72 h. Annealing alone is not sufficient to remove sputter damage with bulk doublet at 64% of the total area.

FIG. 6. (a) XPS spectrum of the P 2p region for an InGaP sample that was etched for 100 ALE cycles after sputtering at 2 keV. Signature of sputter damage has largely been eliminated with bulk doublet comprising 88% of the total area. (b) XPS P 2p spectrum of an InGaP sample that was sputtered for 15 min with 2 keV Ar⁺ ions with no further processing. Bulk doublet is 19% of the total area.

measured for the HF/DMAC process with unspattered reference samples, the etched depth after 25 HF/TMA cycles and 75 HF/DMAC cycles is expected to be ~5–6 nm.

The results in Fig. 6(a) stand in contrast to the results in Fig. 6(b) for the XPS spectrum for an InGaP sample sputtered for 15 min at 2 keV with no further processing. In this case, the more

aggressive sputtering yields an XPS spectrum with larger shifted components than after 500 eV sputtering. The bulk doublet is reduced to 19% of the area after 2 keV sputtering versus 34% of the area after 500 eV sputtering.

Similar experiments were performed for samples sputtered at 2 keV and then etched for 50, 75, and 100 ALE cycles. Figure 7 displays the area of the shifted XPS components as a fraction of

10 October 2024 05:44:36

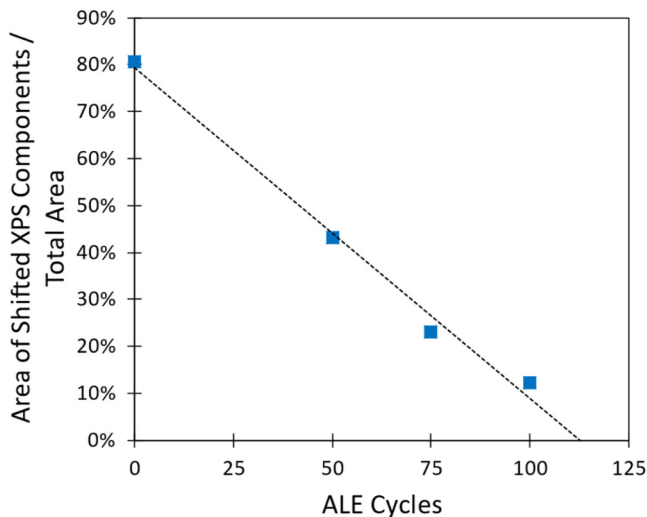


FIG. 7. Area of shifted, nonbulk XPS components as a fraction of the total envelope area for samples sputtered at 2 keV and then etched for a given number of ALE cycles using the standard process. Results show a steady decrease in shifted components with etching and removal of the damaged material.

the total area versus ALE cycles. The area of the shifted XPS components was found to decrease approximately linearly with the number of ALE cycles. Intermediate amounts of etching cause a partial removal of the damaged material. Progressively more bulk material is detected for more ALE cycles. However, sputtering with higher energy ions at 2 keV causes more extensive damage deeper into the crystal. The area of the shifted XPS components for sputtering at 2 keV is still 12% after 100 ALE cycles. In contrast, for sputtering at 500 eV, the area of the shifted XPS components is 4% after 50 ALE cycles in Fig. 5(a).

Given that photoelectrons from P 2p are near the minimum of the universal electron mean free path curve,⁶¹ these XPS results for P 2p are very surface sensitive. Bulk material after 50 and 75 ALE cycles would not be detected if the starting thickness of the damaged material was much larger than 5–6 nm. Therefore, the etch rate for sputtered InGaP does not appear to greatly exceed the etch rate for undamaged material despite the disruption of the crystal lattice.

D. AES results versus the number of ALE cycles

In vacuo AES can be used to monitor Ar implanted into the sample by sputtering and to track the removal of sputter damage. Figure 8 shows the AES Ar atomic percent (at.%) for an InGaP sample that was sputtered at 2 keV and then etched for 50, 75, and 100 ALE cycles using the standard process. The AES Ar at.% decreases linearly with the number of ALE cycles. The AES Ar at.% is completely removed after 100 cycles.

The results in Fig. 8 indicate that the damaged material has been removed after etching ~5–6 nm of InGaP. This trend is in good agreement with the decrease in shifted XPS components

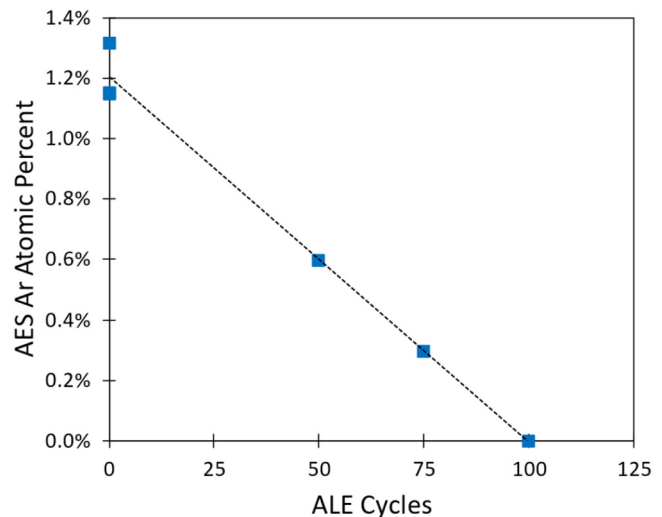


FIG. 8. AES Ar at.% versus the number of ALE cycles after Ar implantation at 2 keV. AES Ar at.% is zero at 100 ALE cycles after etching 5–6 nm of InGaP.

versus ALE cycles observed in Fig. 7. This analysis of AES Ar at.% was also performed after sputtering at 500 eV. In this case, the Ar implantation depth was so shallow that Ar was not detected even after minimal etching with ten HF/TMA ALE cycles.

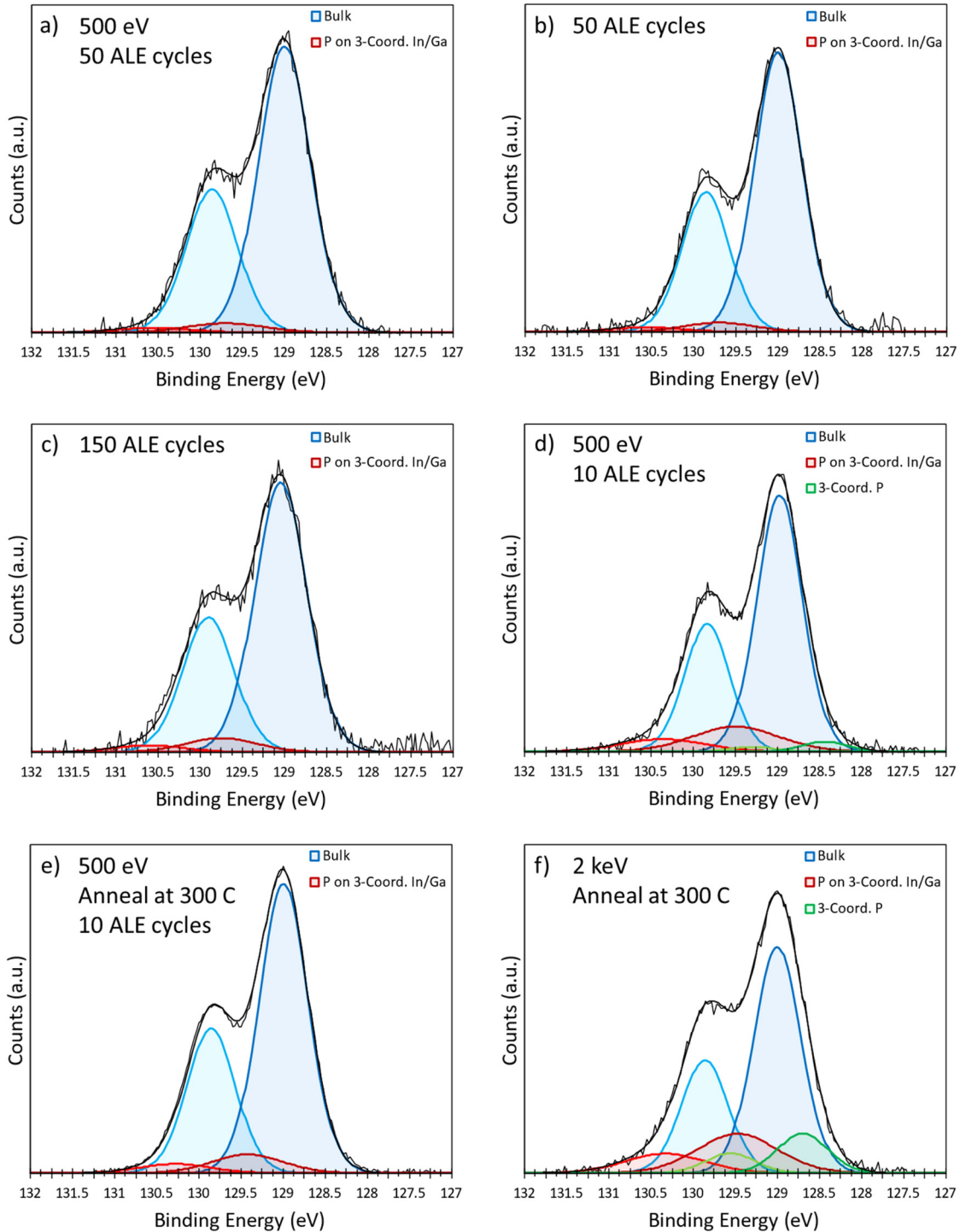
E. Additional XPS results and DFT simulations under different conditions

Figure 9 displays the XPS spectra for different conditions and control experiments. Figure 9(a) is a replication of the same 50 ALE cycle experiment shown in Fig. 5(a). Nearly identical results were observed with 95% of the XPS envelope occupied by the bulk doublet and no implanted Ar detected by AES after ALE. Figure 9(b) shows the results for a control sample that was not sputtered before etching for 50 ALE cycles. The XPS spectrum is unchanged after etching with the bulk doublet occupying 95% of the area. Figure 9(c) illustrates that an additional 100 ALE cycles did not produce changes in the XPS spectrum.

In contrast to the 50 ALE cycle results displayed in Figs. 9(a) and 9(d) shows results for a sample sputtered at 500 eV and then etched for only 10 ALE cycles with the HF/TMA process. The XPS spectrum retained detectable sputter damage with the bulk doublet occupying 82% of the total area. A minimal amount of etching was only partially effective at removing the damaged material. However, no implanted Ar was detected by AES after ten ALE cycles. These results indicate that minimal etching with HF/TMA is more effective than annealing alone as shown in Fig. 5(b).

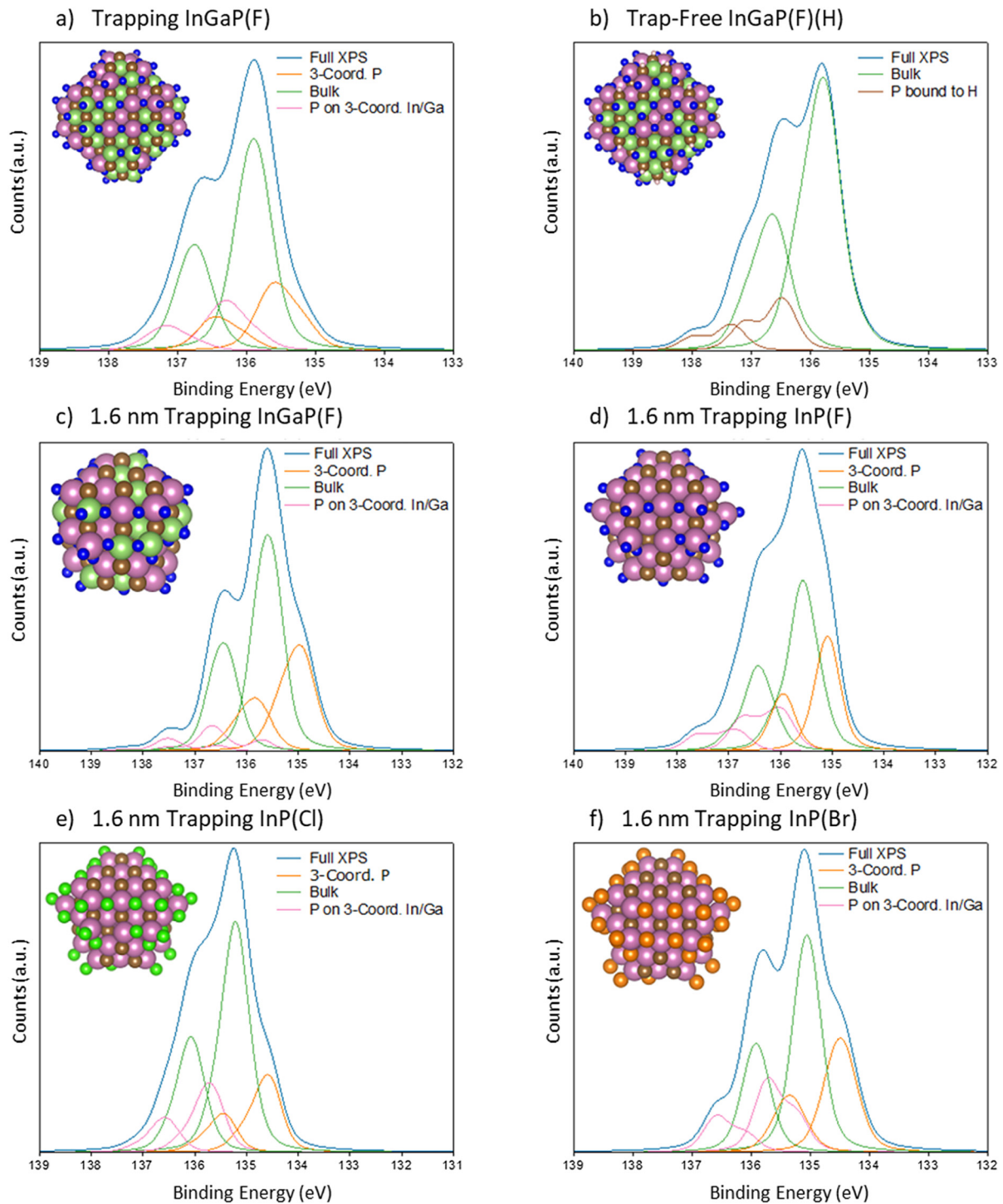
For comparison, Fig. 9(e) displays a 500 eV sputtered sample that was annealed at 300 °C for 24 h before etching for ten ALE cycles with the HF/TMA process. Unlike the trials with either ten ALE cycles or 72 h of annealing alone, this combination of

10 October 2024 05:44:36



10 October 2024 05:44:36

FIG. 9. XPS P 2p spectra of InGaP samples after the following treatments: (a) sputtered at 500 eV and then etched at 300 °C using the standard process for 50 ALE cycles (25 cycles HF/TMA then 25 cycles HF/DMAC). (b) Not sputtered, etched for 50 ALE cycles. (c) Not sputtered, etched for 150 ALE cycles. (d) Sputtered at 500 eV and then etched for ten ALE cycles using HF/TMA only. (e) Sputtered at 500 eV and annealed at 300 °C under 1 Torr N₂ purge for 24 h, then etched for ten ALE cycles using HF/TMA only. (f) Sputtered at 2 keV and then annealed at 300 °C under 1 Torr N₂ purge for 7 days.



10 October 2024 05:44:36

FIG. 10. Predicted XPS spectra for the following nanocrystals: (a) trapping InGaP(F); (b) trap-free InGaP(F)(H); (c) 1.6 nm trapping InGaP(F); (d) 1.6 nm trapping InP(F); (e) 1.6 nm trapping InP(Cl); and (f) 1.6 nm trapping InP(Br). Space-filling model of each nanocrystal is inset in its respective spectra with pink atoms corresponding to indium, light green atoms corresponding to gallium, brown atoms corresponding to phosphorus, blue atoms corresponding to fluorine, bright green atoms corresponding to chlorine, and orange atoms corresponding to bromine. (Color online).

annealing and etching was more effective at removing sputter damage. The bulk doublet in Fig. 9(e) occupied 91% of the total area after processing. Similar to the ten ALE cycle experiment, AES did not detect remaining Ar. Figure 9(f) shows the results for annealing for 7 days at 300 °C after sputtering at 2 keV. This procedure was not effective at removing the surface damage as the bulk doublet was only 68% of the total area. Remaining Ar was also detected by AES after annealing.

The XPS spectra of several additional nanocrystal models were also simulated to assess the validity of the shifts in P 2p CEBE predicted by the DFT procedure. These additional XPS spectra provide insight into the effects of the halogen ligand and the size of the nanocrystal model. These XPS spectra also show the effect of material change from InGaP to InP on the P 2p CEBE.

Figure 10(a) shows the XPS spectrum for an $\text{In}_{68}\text{Ga}_{67}\text{P}_{104}\text{F}_{93}^{0+}$ nanocrystal that is analogous to the structure shown in Fig. 3(b) with all Cl substituted with F. Figure 10(b) displays the XPS spectrum for an $\text{In}_{68}\text{Ga}_{67}\text{P}_{104}\text{F}_{117}\text{H}_{24}^{0+}$ nanocrystal starting from the nanocrystal in Fig. 10(a) where all P-3c are passivated by protons. The nanocrystal is charge balanced by an overabundance of F^- used to passivate all In/Ga-3c. Like the results shown in Fig. 3(a), the peak for this structure is narrower than the peak for the defected nanocrystals, but additional broadening arises from a shift to higher CEBE by the protonated P atoms. Figure 10(c) displays the XPS spectrum for a smaller $\text{In}_{28}\text{Ga}_{27}\text{P}_{40}\text{F}_{45}^{0+}$ nanocrystal. This nanocrystal is a 1.6 nm asymmetric, roughly cuboctohedral nanocrystal with (100) and (111) facets on the surface.

Figure 10(d) shows the XPS spectrum for an $\text{In}_{55}\text{P}_{40}\text{F}_{45}^{0+}$ nanocrystal that is an InP analog to the InGaP nanocrystal in Fig. 10(c). Figure 10(e) displays the XPS spectrum for an $\text{In}_{55}\text{P}_{40}\text{Cl}_{45}^{0+}$ nanocrystal that is analogous to the nanocrystal in Fig. 10(d) with all F substituted by Cl. Finally, Fig. 10(e) shows the results for an $\text{In}_{55}\text{P}_{40}\text{Br}_{45}^{0+}$ nanocrystal that is analogous to the nanocrystal in Fig. 10(d) with all F substituted by Br.

There are some general trends that emerge from these predicted XPS spectra. For all defected nanocrystals, phosphorus atoms bound to three-coordinate indium or gallium are shifted to higher CEBEs. Likewise, the three-coordinate phosphorus atoms are shifted to lower CEBEs. The bulk P 2p CEBEs are higher for the halogen ligands with larger electronegativities. The P 2p_{1/2} bulk CEBEs are 135.9, 136.1, and 136.5 eV for the Br, Cl, and F ligands, respectively. However, further work is necessary to fully investigate such trends in the XPS peak position.

IV. CONCLUSIONS

Compound semiconductors such as aluminum indium gallium phosphide (AlInGaP) are widely used for LED devices. Surface defects on LED devices can lead to nonradiative electron/hole pair recombination that reduces their light output. Some of the surface defects are believed to be formed by energetic ion species from plasma processing used to fabricate the LEDs. Thermal ALE may provide a method to remove these surface defects.

Thermal ALE was conducted using a new apparatus that combines a hot-wall ALE reactor with *in vacuo* Auger electron spectroscopy (AES). This apparatus allows the sample to be characterized throughout the thermal ALE process without exposure

to air. InGaP was employed to model AlInGaP quaternary phosphide. InGaP thermal ALE was performed using static, sequential fluorination, and ligand-exchange reaction using hydrogen fluoride (HF) and either trimethylaluminum (TMA) or DMAC exposures. The HF/TMA process removed any oxide layer present on the sample and the HF/DMAC process etched the underlying bulk InGaP material with an etch rate of $\sim 0.7 \text{ \AA/cycle}$ at a temperature of 300 °C.

The removal of surface defects by ALE was studied using *ex situ* XPS. InGaP samples damaged by Ar^+ ion sputtering were analyzed before and after thermal ALE by tracking the shifted components in the P 2p XPS region that correspond to damage from sputtering. An XPS scan of an unsputtered InGaP sample showed only a bulk doublet. An InGaP sample after sputtering displayed two additional shifted doublets. DFT calculations identified the surface damage as undercoordinated atoms in the InGaP lattice. Higher binding energies were assigned to phosphorus atoms directly bound to three-coordinate indium or gallium. Lower binding energies were associated with three-coordinate phosphorus.

InGaP thermal ALE can then remove the XPS features associated with the damaged lattice. A bulklike XPS spectrum showing minimal damage was obtained after 50 ALE cycles for a sample initially exposed to 500 eV sputtering. By contrast, annealing for 72 h at 300 °C without etching was not sufficient to eliminate damage. AES analysis similarly showed that Ar implanted in the sample by sputtering was removed after etching but not annealing. Increasing the sputtering ion energy to 2 keV required more extensive etching to remove sputter damage. With the higher ion energy of 2 keV, XPS and AES both indicated that 100 ALE cycles were able to largely remove the surface defects. The etch depth consistent with 100 ALE cycles indicates a damaged material depth of $\sim 5\text{--}6 \text{ nm}$.

ACKNOWLEDGMENTS

This work was supported by the Joint University Microelectronics Program (JUMP) funded by the Semiconductor Research Corporation (SRC).

AUTHOR DECLARATIONS

Conflict of Interest

The authors have no conflicts to disclose.

Author Contributions

Ross Edel: Data curation (lead); Formal analysis (lead); Investigation (lead); Writing – original draft (lead); Writing – review & editing (equal). **Ezra Alexander:** Data curation (equal); Formal analysis (supporting); Investigation (supporting); Writing – original draft (supporting); Writing – review & editing (supporting). **Taewook Nam:** Data curation (supporting); Investigation (supporting). **Andrew S. Cavanagh:** Data curation (equal). **Troy Van Voorhis:** Methodology (equal); Supervision (equal); Writing – review & editing (supporting). **Steven M. George:** Conceptualization (lead); Funding acquisition (lead); Methodology (equal); Project administration (lead); Supervision (equal); Writing – review & editing (equal).

DATA AVAILABILITY

The data that support the findings of this study are available within the article.

REFERENCES

¹Th. Gessmann and E. F. Schubert, *J. Appl. Phys.* **95**, 2203 (2004).
²O. A. Fedorova, K. A. Bulashevich, and S. Y. Karpov, *Opt. Express* **29**, 35792 (2021).
³M. S. Wong *et al.*, *Opt. Express* **28**, 5787 (2020).
⁴M. Boroditsky *et al.*, *J. Appl. Phys.* **87**, 3497 (2000).
⁵K. A. Bulashevich and S.Yu. Karpov, *Phys. Status Solidi RRL* **10**, 480 (2016).
⁶P. Royo, R. P. Stanley, M. Ilegems, K. Streubel, and K. H. Gulden, *J. Appl. Phys.* **91**, 2563 (2002).
⁷J.-T. Oh *et al.*, *Opt. Express* **26**, 11194 (2018).
⁸Y. Boussadi, N. Rochat, J.-P. Barnes, B. B. Bakir, P. Ferrandis, B. Masenelli, and C. Licitra, *J. Lumin.* **234**, 117937 (2021).
⁹K. Fan *et al.*, *Opt. Express* **31**, 36293 (2023).
¹⁰J. Kou *et al.*, *Opt. Express* **27**, A643 (2019).
¹¹S. S. Konoplev, K. A. Bulashevich, and S.Yu. Karpov, *Phys. Status Solidi A* **215**, 1700508 (2018).
¹²L. Yu *et al.*, *Appl. Phys. Lett.* **121**, 042106 (2022).
¹³S. Miyakuni, R. Hattori, K. Sato, H. Takano, and O. Ishihara, *J. Appl. Phys.* **78**, 5734 (1995).
¹⁴B. O. Jung, W. Lee, J. Kim, M. Choi, H.-Y. Shin, M. Joo, S. Jung, Y.-H. Choi, and M. J. Kim, *Sci. Rep.* **11**, 4535 (2021).
¹⁵J.-H. Park, M. Pristovsek, W. Cai, H. Cheong, A. Tanaka, Y. Furusawa, D.-P. Han, T.-Y. Seong, and H. Amano, *Adv. Opt. Mater.* **11**, 2203128 (2023).
¹⁶H. W. Dinges, B. Kempf, and H. Burkhard, *Surf. Interface Anal.* **16**, 77 (1990).
¹⁷G. Greczynski and L. Hultman, *Appl. Surf. Sci.* **542**, 148599 (2021).
¹⁸W. M. Lau, R. N. S. Sodhi, B. J. Flinn, K. H. Tan, and G. M. Bancroft, *Appl. Phys. Lett.* **51**, 177 (1987).
¹⁹M. C. López-Escalante, M. Gabás, I. García, E. Barrigón, I. Rey-Stolle, C. Algora, S. Palanco, and J. R. Ramos-Barrado, *Appl. Surf. Sci.* **360**, 477 (2016).
²⁰E. Lewin, M. Gorgoi, F. Schäfers, S. Svensson, and U. Jansson, *Surf. Coat. Technol.* **204**, 455 (2009).
²¹J. Sundberg, R. Lindblad, M. Gorgoi, H. Rensmo, U. Jansson, and A. Lindblad, *Appl. Surf. Sci.* **305**, 203 (2014).
²²N. A. Besley, *Acc. Chem. Res.* **53**, 1306 (2020).
²³S. Han, C. Xu, H. Li, S. Liu, H. Xu, Y. Zhu, A. Fang, and X. Wang, *Opt. Mater.* **114**, 110860 (2021).
²⁴M. S. Wong, R. C. White, S. Gee, T. Tak, S. Gandrothula, H. Choi, S. Nakamura, J. S. Speck, and S. P. DenBaars, *Appl. Phys. Express* **16**, 066503 (2023).
²⁵Y. Yang and X. A. Cao, *J. Vac. Sci. Technol. B* **27**, 2337 (2009).
²⁶S. Zhang, Q. Fan, X. Ni, L. Tao, and X. Gu, *Crystals* **13**, 1611 (2023).
²⁷T.-Y. Seong and H. Amano, *Surf. Interfaces* **21**, 100765 (2020).
²⁸M.-J. Jeng, Y.-H. Chang, L.-B. Chang, M.-J. Huang, and J.-C. Lin, *Jpn. J. Appl. Phys.* **46**, L291 (2007).
²⁹J. Park, W. Baek, D.-M. Geum, and S. Kim, *Nanoscale Res. Lett.* **17**, 29 (2022).
³⁰S. M. George, *Acc. Chem. Res.* **53**, 1151 (2020).

³¹T. Faraz, F. Roozeboom, H. C. M. Knoops, and W. M. M. Kessels, *ECS J. Solid State Sci. Technol.* **4**, N5023 (2015).
³²S. M. George, *Chem. Rev.* **110**, 111 (2010).
³³K. J. Kanarik, T. Lill, E. A. Hudson, S. Sriraman, S. Tan, J. Marks, V. Vahedi, and R. A. Gottscho, *J. Vac. Sci. Technol. A* **33**, 020802 (2015).
³⁴J. W. Elam, M. D. Groner, and S. M. George, *Rev. Sci. Instrum.* **73**, 2981 (2002).
³⁵S. Mroczkowski and D. Lichtman, *J. Vac. Sci. Technol. A* **3**, 1860 (1985).
³⁶P. Petrik and M. Fried, "Ellipsometry of semiconductor nanocrystals," in *Ellipsometry at the Nanoscale*, edited by M. Losurdo and K. Hingerl (Springer, Berlin, 2013).
³⁷A. M. Cano, A. E. Marquardt, J. W. DuMont, and S. M. George, *J. Phys. Chem. C* **123**, 10346 (2019).
³⁸Y. Lee, J. W. DuMont, and S. M. George, *Chem. Mater.* **28**, 2994 (2016).
³⁹Y. Lee, C. Huffman, and S. M. George, *Chem. Mater.* **28**, 7657 (2016).
⁴⁰J. W. Clancey, A. S. Cavanagh, J. E. T. Smith, S. Sharma, and S. M. George, *J. Phys. Chem. C* **124**, 287 (2020).
⁴¹Y. Lee and S. M. George, *J. Phys. Chem. C* **123**, 18455 (2019).
⁴²W. Lu, Y. Lee, J. C. Gertsch, J. A. Murdzek, A. S. Cavanagh, L. Kong, J. A. del Alamo, and S. M. George, *Nano Lett.* **19**, 5159 (2019).
⁴³T. J. Myers, A. M. Cano, D. K. Lancaster, J. W. Clancey, and S. M. George, *J. Vac. Sci. Technol. A* **39**, 021001 (2021).
⁴⁴T. Goldzak, A. R. McIsaac, and T. Van Voorhis, *Nat. Commun.* **12**, 890 (2021).
⁴⁵N. Geva, J. J. Shepherd, L. Nienhaus, M. G. Bawendi, and T. Van Voorhis, *J. Phys. Chem. C* **122**, 26267 (2018).
⁴⁶T. D. Kühne *et al.*, *J. Chem. Phys.* **152**, 194103 (2020).
⁴⁷N. A. Besley, A. T. B. Gilbert, and P. M. W. Gill, *J. Chem. Phys.* **130**, 124308 (2009).
⁴⁸Y. Shao *et al.*, *Mol. Phys.* **113**, 184 (2015).
⁴⁹A. T. B. Gilbert, N. A. Besley, and P. M. W. Gill, *J. Phys. Chem. A* **112**, 13164 (2008).
⁵⁰W. L. Jolly, K. D. Bomben, and C. J. Eyermann, *At. Data Nucl. Data Tables* **31**, 433 (1984).
⁵¹T. M. Henderson, B. G. Janesko, and G. E. Scuseria, *J. Chem. Phys.* **128**, 194105 (2008).
⁵²A. V. Krukau, O. A. Vydrov, A. F. Izmaylov, and G. E. Scuseria, *J. Chem. Phys.* **125**, 224106 (2006).
⁵³F. Weigend and R. Ahlrichs, *Phys. Chem. Chem. Phys.* **7**, 3297 (2005).
⁵⁴B. Metz, H. Stoll, and M. Dolg, *J. Chem. Phys.* **113**, 2563 (2000).
⁵⁵B. P. Pritchard, D. Altarawy, B. Didier, T. D. Gibson, and T. L. Windus, *J. Chem. Inf. Model.* **59**, 4814 (2019).
⁵⁶D. Feller, *J. Comput. Chem.* **17**, 1571 (1996).
⁵⁷K. L. Schuchardt, B. T. Didier, T. Elsethagen, L. Sun, V. Gurumoorhi, J. Chase, J. Li, and T. L. Windus, *J. Chem. Inf. Model.* **47**, 1045 (2007).
⁵⁸T. J. Väyrynen, T. A. Kaurila, R. G. Cavell, and K. H. Tan, *J. Electron Spectrosc. Relat. Phenom.* **61**, 55 (1992).
⁵⁹R. G. Cavell and K. H. Tan, *Chem. Phys. Lett.* **197**, 161 (1992).
⁶⁰E. Alexander, M. Kick, A. R. McIsaac, and T. Van Voorhis, *Nano Lett.* **24**, 7227 (2024).
⁶¹M. P. Seah and W. A. Dench, *Surf. Interface Anal.* **1**, 2 (1979).

10 October 2024 05:44:36